


Global stability analysis of an idealized compressor blade row. II. Multiple-blade interactions

Anton Glazkov

Mechanical Engineering, Physical Science and Engineering Division, KAUST, Thuwal 23955, Saudi Arabia

Miguel Fosas de Pando

*Departamento Ingeniería Mecánica y Diseño Industrial, Escuela Superior de Ingeniería,
Universidad de Cádiz, Puerto Real 11519, Spain*

Peter J. Schmid *

Mechanical Engineering, Physical Science and Engineering Division, KAUST, Thuwal 23955, Saudi Arabia

Li He

Department of Engineering Science, University of Oxford, Oxford OX1 3PJ, United Kingdom



(Received 13 December 2022; accepted 25 May 2023; published 11 October 2023)

A direct-adjoint mean flow global stability investigation of self-excited instabilities in an idealized, two-dimensional compressor blade row at off-design conditions is carried out. In this second part of the paper, the single-passage analysis is extended to multi-blade passages by exploiting the properties of block-circulant matrices and Bloch-wave theory. By using this method, analyses for a large number of blade passages become computationally tangible, and the modal and nonmodal single-passage analysis from the first part of the paper can be augmented by considering multiblade effects arising in larger systems. This work shows that multiblade passages introduce additional unstable 10- and five-periodic synchronization structures arising from a tuned optimal phase relationship that is supported by the larger system. Self-excited low-frequency structures, which cannot be represented within a single-passage computation, are also uncovered and analyzed.

DOI: [10.1103/PhysRevFluids.8.103904](https://doi.org/10.1103/PhysRevFluids.8.103904)

I. INTRODUCTION

With turbomachinery blade rows consisting of multiple periodic structural elements interacting with the flow, it is natural to consider extensions of the global stability problem, as presented in part I of this paper [1], to N passages. In this way, the large-scale behavior throughout the full blade row, that previously could not be modeled with the restriction to a single-passage periodic domains, is captured. Unfortunately, global stability analysis becomes intractable, even in situations when N is relatively small (e.g., $N < 5$), and so the problem must be simplified in some way to account

*Corresponding author: peter.schmid@kaust.edu.sa

Published by the American Physical Society under the terms of the [Creative Commons Attribution 4.0 International](https://creativecommons.org/licenses/by/4.0/) license. Further distribution of this work must maintain attribution to the author(s) and the published article's title, journal citation, and DOI. Open access publication funded by King Abdullah University of Science and Technology.

for this periodicity without increasing the instantaneous demand for computer resources. This difficulty has been addressed previously using the harmonic balance method [2–5], phase-lagged [6–8], and chorochronic approaches [9] to account for the periodicity in blade-row simulations, although note that none of these can account for self-excited instabilities as the formulations of these approaches are subject to prescribed phase-shift periodicities of *known* frequencies. More recently, in [10] a fully algebraic linear approach was proposed, where the direct system matrix is rearranged into block-circulant form by reconfiguration of the state vector. Assumptions made regarding the numerical nearest-neighbor coupling¹ of the blade passages can be exploited to increase the sparsity of the linear operator without compromising any physical dynamics. This approach is reminiscent of Bloch-wave theory [11], and similar methods have been used in the past, for example, in the field of structural mechanics to study vibrations in bladed disks [12]. The diversity of potential applications was demonstrated in [10], treating the dynamics in periodic viscous wakes, annular combustors, burners and blade rows as examples. In the latter instance, a 54-blade linear cascade was studied in the context of incompressible flow, with a continuously parameterized spectrum obtained alongside optimal forcing and response structures. In this paper we seek to extend this approach to a fully compressible flow problem with the aim of identifying the macrodynamics originating from the feedback mechanisms linking the microscale self-excited hydrodynamics processes and the propagating acoustics field. Perhaps the closest analog of this in turbomachinery applications are compressor nonengine order vibration phenomena [13] and acoustic resonance structures [14–17], which have been suggested to occur as a consequence of vortex shedding from separation bubbles forming on the suction surfaces of the compressor blades when operating at off-design conditions.

The geometry and flow conditions are identical to those presented in part I, so that a comparison between the single and multiple passage cases can be made.

This paper builds upon the work of part I, by extending the earlier global stability analysis to a 10-periodic blade row using the algebraic method introduced in [10] in Sec. II. Details of the geometry and implementation are provided in Secs. II A and II B, respectively. This is followed once again by an impulse response analysis in Sec. II C, and global stability analysis in Sec. II D, where we observe structures that arise in the larger domain. To complete the discussion, Sec. III summarizes the findings and provides possible extensions and future perspectives of this work.

II. MULTIPLE PASSAGES

So far in this work we have focused on the single-passage dynamics, which has provided us valuable insight into the local stability characteristics of the flow over a single blade. Realistic annular blade rows, however, typically contain on the order of 10 to 50 blade passages and are capable of supporting large-wavelength disturbances, synchronization and standing waves that are impossible to resolve in a simulation of a single periodic passage. In this section, we consider a 10-passage configuration and extend the global stability analysis above to this case. We achieve this by using a N -periodic matrix decomposition method that allows large system matrices to be decomposed into smaller independent problems that are simpler to solve.

A. N -periodic geometry

For the purpose of this study, we will restrict ourselves to a 10-passage linear cascade, and make use of the model controlled-diffusion compressor passage geometry from part I that is tessellated in the vertical direction as shown in Fig. 1. Periodic boundary conditions are applied in the upstream and downstream regions of the mesh corresponding to passages P_0 and P_9 .

¹In other words, the code enforces the coupling, but, by construction, communications in the code occur only between neighboring passages.

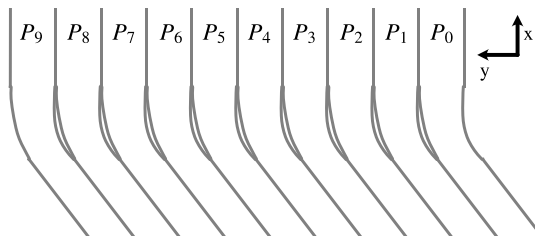


FIG. 1. The physical 10-passage geometry considered in this section. The axial lengths of the upstream and downstream sections of this geometry have been chosen so that wavelengths of up to $5h_p$ could be represented within the simulation.

B. N -periodic modeling

While in theory it is possible to model entire N -periodic configurations directly simply by modeling N blade passages in a single mesh, this approach becomes impractical as the number of passages is increased. This limitation arises independently of the parallel scaling performance of the code, since the main constraints come from having to store large snapshots of data for the Krylov-Schur algorithm in random-access memory (RAM), and finding computational resources on which instantaneous access to $N \times$ (number of processors per passage) processors is available for extended periods of time. More pertinent to the analysis itself, however, is that larger time intervals between the snapshots may be required to converge the low-frequency modes with the exponential time-stepping method, since with larger blade counts, structures with very low azimuthal wavenumbers and low temporal frequencies are expected, resulting in convergence issues without prior adjustment of the time step. Although this may seem like a hopeless endeavour, by making a few sufficiently general assumptions these issues are easily mitigated.

Linearizing the N -periodic system we arrive at the initial-value problem (IVP)

$$\frac{d\mathbf{v}}{dt} = \mathbf{A}\mathbf{v}, \quad \mathbf{v}(0) = \mathbf{v}_0, \quad (1)$$

where \mathbf{A} and \mathbf{v} represent the $nN \times nN$ and nN size matrix and vector, respectively, with n being the total degrees of freedom in each passage and N the number of passages.

We make two assumptions about this system:

- (1) That the blade surface geometries, and by extension the meshes, for each passage are identical and
- (2) That the mean flow within each passage is the same.

Grouping the entries of \mathbf{A} and \mathbf{v} by passages, such that $\mathbf{v} = (\mathbf{v}_0, \mathbf{v}_1, \dots, \mathbf{v}_{N-1})^T$, with \mathbf{v}_j denoting the portion of the state vector in the j th passage, under these assumptions, transforms the state matrix into block-circulant form

$$\mathbf{A} = \begin{pmatrix} \mathbf{A}_0 & \mathbf{A}_1 & \cdots & \mathbf{A}_{N-1} \\ \mathbf{A}_{N-1} & \mathbf{A}_0 & \cdots & \mathbf{A}_{N-2} \\ \vdots & \ddots & \ddots & \vdots \\ \mathbf{A}_1 & \cdots & \mathbf{A}_{N-1} & \mathbf{A}_0 \end{pmatrix}. \quad (2)$$

We can interpret this form of \mathbf{A} as the local dynamics of a given passage in \mathbf{v}_j , governed by \mathbf{A}_0 , and the influence of all other passages $\mathbf{v}_{i \neq j}$ effected through the off-diagonal matrices $\mathbf{A}_{i \neq 0}$ on the dynamics of \mathbf{v}_j , so that

$$\frac{d\mathbf{v}_j}{dt} = \mathbf{A}_0\mathbf{v}_j + \sum_{i \neq j} \mathbf{A}_{(i-j) \bmod N} \mathbf{v}_i. \quad (3)$$

In other words, the number of off-diagonal nonzero blocks is determined by the spatial coupling between the j th passage and its neighbours. Generally, this is imposed by the spatial differentiation scheme as in the case of finite-difference and finite-volume schemes, or through the boundary nodes of neighboring elements in a finite-element formulation, for example.

Many applications, including this present one, exhibit either nearest-neighbor coupling or a weak global coupling. This means that the only passages that contribute to the solution are the dynamics in the passage above and below.² Hence, Eq. (2) becomes a *block-tridiagonal* system with only \mathbf{A}_{N-1} , \mathbf{A}_0 and $\mathbf{A}_1 \neq 0$. Although smaller, the system is not yet decoupled, however, and further manipulation is required to make progress.

Fortunately, among the many properties of circulant matrices is the diagonalization transformation that takes a block-circulant matrix into block diagonal form (see, e.g., [10]). Picking the matrices so that $\mathbf{J} \in \mathbb{C}^{N \times N}$ and $\mathbf{P} \in \mathbb{C}^{nN \times nN}$,

$$\mathbf{J}_{j+1,k+1} = \rho_j^k / \sqrt{N}, \quad \rho = e^{2\pi i j / N} \quad (4)$$

$$\mathbf{P} = \mathbf{J} \otimes \mathbf{I}_{n \times n}, \quad (5)$$

and for any matrix function, f , of the system matrix, we can diagonalize according to

$$\mathbf{P}^H f(\mathbf{A}) \mathbf{P} = f(\hat{\mathbf{A}}), \quad (6)$$

where

$$f(\hat{\mathbf{A}}) = \begin{pmatrix} f(\hat{\mathbf{A}}_0) & & & \\ & f(\hat{\mathbf{A}}_1) & & \\ & & \ddots & \\ & & & f(\hat{\mathbf{A}}_{N-1}) \end{pmatrix} \quad (7)$$

and moreover,

$$\hat{\mathbf{A}}_j = \mathbf{A}_0 + \rho_j \mathbf{A}_1 + 1/\rho_j \mathbf{A}_{N-1}. \quad (8)$$

In a matrix-free setting we are only concerned with matrix-vector products such as $\hat{\mathbf{A}}_j \hat{\mathbf{v}}_j$, and so from Eq. (8), it is clear that this amounts to taking the three matrix-vector products $\mathbf{A}_0 \hat{\mathbf{v}}_j$, $\mathbf{A}_1 \hat{\mathbf{v}}_j$ and $\mathbf{A}_{N-1} \hat{\mathbf{v}}_j$.

While performing each of these calculations individually is possible, to reduce the computational overhead, we instead linearise around a three-passage geometry with identical mean flows in each passage, giving a $3n \times 3n$ block-circulant matrix

$${}^3\mathbf{A} = \begin{pmatrix} \mathbf{A}_0 & \mathbf{A}_{N-1} & \mathbf{A}_1 \\ \mathbf{A}_1 & \mathbf{A}_0 & \mathbf{A}_{N-1} \\ \mathbf{A}_{N-1} & \mathbf{A}_1 & \mathbf{A}_0 \end{pmatrix}. \quad (9)$$

Multiplying by the augmented vector ${}^3\hat{\mathbf{v}}_j = (\mathbf{0}, \hat{\mathbf{v}}_j, \mathbf{0})$ gives

$${}^3\mathbf{A}({}^3\hat{\mathbf{v}}_j) = \begin{pmatrix} \mathbf{A}_{N-1} \hat{\mathbf{v}}_j \\ \mathbf{A}_0 \hat{\mathbf{v}}_j \\ \mathbf{A}_1 \hat{\mathbf{v}}_j \end{pmatrix}, \quad (10)$$

which is now easy to combine into the form of Eq. (8). Assuming that all passages have the same processor distributions, the local solution of the top and bottom passage is simply transferred to

²In the case of weak global coupling, assuming nearest-neighbor coupling would introduce a small error. Indeed, in many numerical codes spatial coupling is introduced through the derivative, which is known to be an essentially local property. Therefore, if the passage height between blades is sufficiently large, this error will typically be below that of machine precision. Note that this is an assumption about the structure of the code, not the physical system.

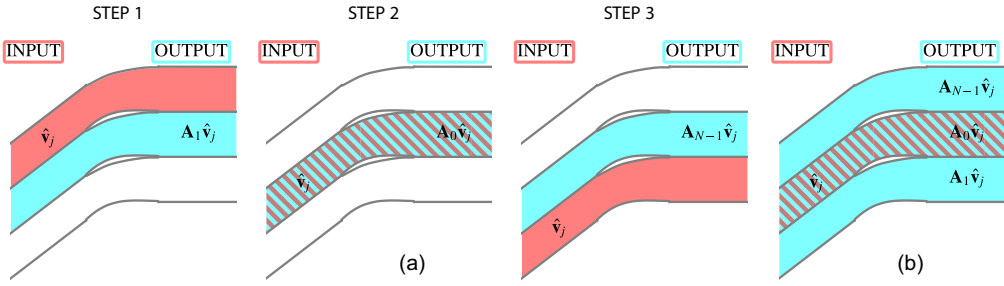


FIG. 2. Evaluation of the matrix-vector product $\hat{\mathbf{A}}_j \hat{\mathbf{v}}_j$ using a three-pass linearization. The three-stage direct approach making use of sequential matrix-vector evaluation in (a) can be simplified in (b) by combining the three stages into one matrix-vector evaluation.

the corresponding processor on the middle passage, premultiplied by ρ_j or ρ_j^{-1} and added to the local solution of the corresponding destination processor (i.e., the processor where the final solution is assembled). This is easily achieved in MPI by using `MPI_Cart_create` and a sequence of `MPI_SendRecv` calls, and has the advantage of using preexisting linear codes with minimal programming intervention required by the end user. A diagram of this procedure is shown in Fig. 2. Figure 3 shows how these coupling fields, $\mathbf{A}_1 \hat{\mathbf{v}}_j$ and $\mathbf{A}_{N-1} \hat{\mathbf{v}}_j$, manifest themselves in the periodic blade row that is considered here. A linearization of the three-pass system is performed and a random field for $\hat{\mathbf{v}}_j$ is introduced into the middle passage. In the figure, the solution in the middle passage is removed to visualize coupling fields, and to demonstrate how these are reintroduced into the central passage. This case also serves as a validation of the adjoint, with a corresponding adjoint matrix-vector product computed and compared using the familiar duality relation, giving a relative error of 4.571×10^{-14} .

In essence, the large original problem in Eq. (1) is recast as N independent three-pass simulation problems, since now we only have to solve problems of the kind

$$\frac{d(\mathbf{v}_j)}{dt} = {}^{3 \rightarrow 1} \mathbf{C}(\mathbf{A})(\mathbf{v}_j), \quad (11)$$

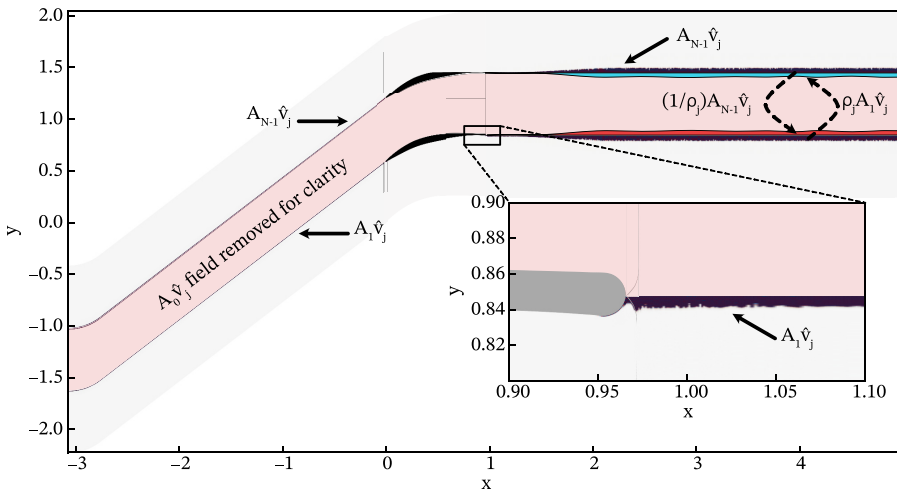


FIG. 3. The coupling fields $\mathbf{A}_1 \hat{\mathbf{v}}_j$ and $\mathbf{A}_{N-1} \hat{\mathbf{v}}_j$ are shown for the computational, three-pass mesh. The assembly procedure taking these fields into the middle passage is also shown.

where the matrix ${}^{3 \rightarrow 1}\mathbf{C}$ represents the communications in Fig. 2(b), the assembly of the sum (8) and zeroing out the top and bottom passages to return the resulting evolution vector to the standard triplet form, in other words: $d({}^3\mathbf{v}_j)/dt = ({}^3d\mathbf{v}_j/dt)$.

Without optimization, the computational cost is nominally three times larger for the full periodic system than the full computation, however these N simulations may be run independently, with lower demands on the computational resources at any given time and with a lower RAM requirement. Further improvements to the overall cost can also be made by carefully examining the exact form of the coupling matrices \mathbf{A}_1 and \mathbf{A}_{N-1} , since these are expected to have substantial sparsity, and also by assessing the code structure that leads to the coupling matrices. As an example of the latter, where ghost regions are used, the coupling matrices are essentially a proxy for the communications between the ghost cells and the interior of the neighboring domain in the triplet. Instead of communicating with the neighboring mesh, however, the procedure can be modified for a single periodic passage so that the ghost-cell portion of the data is intercepted, multiplied by the appropriate root of unity ρ_j and then applied to the destination processors across the periodic boundary. Doing this would bring the total cost from $3N$ to just N as no additional mesh segments have to be considered. On the other hand, the cost of significant additional development time is a consideration that must be taken into account, especially since many existing code structures would have to be rewritten.

In the following we use the same mean flow and passage geometries that have been computed for the single passage to keep the analysis consistent with the work performed earlier in part I. The only alteration between our two cases has been the reduction in the size of the sponge layer, in the linear analysis, from $\Delta x_{\text{sponge}} = 2.0$ to $\Delta x_{\text{sponge}} = 1.0$, so that the larger wavelengths can be represented with reduced dissipation within the domain.³ We compute all the results in this section using the N -periodic decomposition method detailed above.

C. Impulse response analysis

Following the methodology set out in part I, we begin with an impulse response analysis. Since the local dynamics near the blade surface have already been established, we turn our attention instead to the large-scale structures present in this 10-periodic configuration. For ease of comparison, the initial condition is kept identical to the single-passage case but is applied only between the third and fourth passages (P_2 and P_3 in Fig. 1) in the configuration, as shown in the upper left panel of Fig. 4. Of course there is a greater flexibility in this particular case regarding the choice for the exact form of the initial perturbation, but it has been kept consistent with our single-passage response analysis, so that the mechanism by which the instability develops within the perturbed passage, and how it communicates and interacts with the neighboring passages, is made clearer and easier to interpret. The other panels in Fig. 4 show the disturbance evolving over the same $t = 20$ timescale used in the single passage, for an easy comparative analysis.

Initially the perturbation evolves in much the same way as in the single passage, with scattering from the perturbed blade as the disturbance is advected into the path of the aerofoil leading edge. This is followed by the now familiar growth of Tollmien-Schlichting wave packets and the subsequent amplification by the Orr mechanism at the separation bubble. The difference here, at least for $t \leq 1.0$, is that while the convective disturbance is left at the surface of the perturbed aerofoil, the pressure waves scattered from the leading edges can now propagate and interact with neighboring blades, at which point secondary reflections and further scattering of the pressure waves

³This has the effect of marginally increasing $\text{Re}\{\lambda\}$ for M_6 , making it unstable. We should note too that, in the context of a mean flow stability analysis, this small change in growth rates is largely unimportant because the dynamics of the problem are defined predominantly by the frequencies and structures of the global modes rather than the growth rates. Mode frequencies are unaffected by the changes in the parameters of the sponge layer.

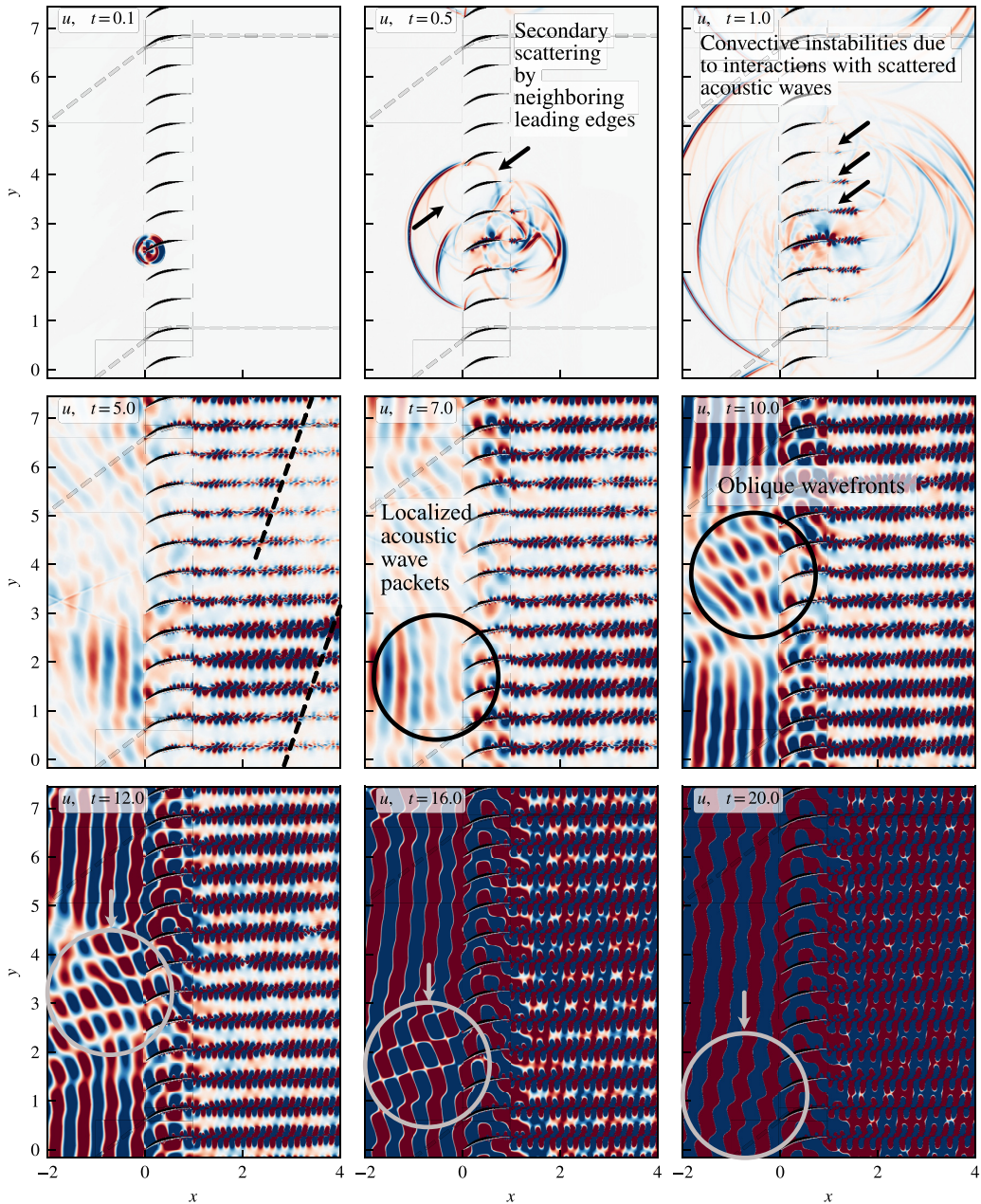


FIG. 4. The evolution of the transient response to the divergence-free perturbation. Also see the animation of the above image sequence in the Supplemental Material [18] (file Part2-Fig4-n-periodic-impulse-response.mp4).

from the other blades can be observed at $t = 0.5$. Furthermore, through the acoustic receptivity mechanisms identified in part I, these secondary scattered waves propagate along the aerofoil surfaces and introduce additional convective instabilities on the affected aerofoils, which can be seen at the trailing edges at $t = 1.0$. These are nevertheless dominated by the blade to which the

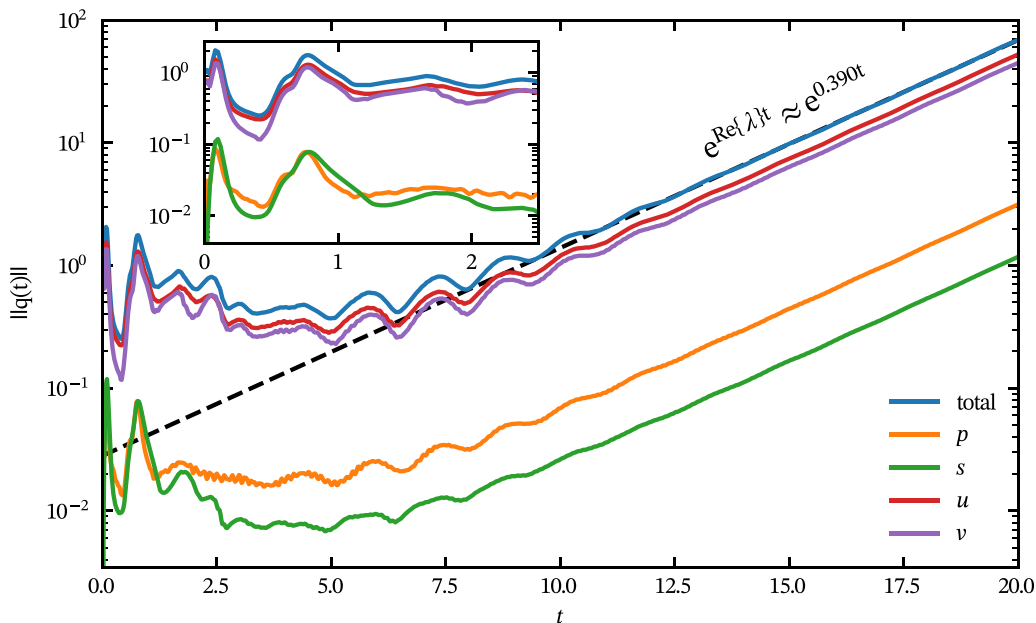


FIG. 5. Evolution of the 10-passage norm, showing the initial transient dynamics for $t = 0 \rightarrow 5$ and the asymptotic regime for $t = 10 \rightarrow \infty$.

perturbation is applied, since most of the energy is retained in the convective structures rather than the scattered acoustic waves of the initial pulse.

When the disturbance reaches the trailing edge, the acoustic source becomes active, which once again occurs at approximately $t = 2$, based on the increase in the pressure component of the norm in Fig. 5 above the level of the entropy component. As before, the acoustic radiation exhibits a directivity that is focused primarily in the upstream direction, resulting in the interaction of the acoustic waves with the regions of sensitivity identified in the wavemaker analysis for the single passage. This time, however, these interactions occur on the perturbed blade as well as on the pressure surface of the blade above and on the suction surface of the blade below. Indeed, aside from the small amounts of scattering of the acoustic waves by the leading and trailing edges of the unperturbed blades, the primary forcing that spreads the initial disturbance to the neighboring passages occurs through this mechanism. This is confirmed by the localized growth of the disturbance despite the acoustic waves propagating through the whole domain at timescales far shorter⁴ than the observed evolution of the perturbation.

As we noted for the single-passage case, both the pressure and suction surfaces have regions of high receptivity to acoustic waves with frequencies associated with the Kelvin-Helmholtz instability (i.e., $\text{Im}\{\lambda\} \approx 31$), with the suction side being the more sensitive of the two regions. Although we expect modifications to the M_0 mode of the single passage, due to the removal of the restrictive single-passage periodicity, we hypothesize—and will later confirm—that the receptivity mechanism for this mode will be similar to those identified in the single-passage analysis, since the mean flow is identical in both cases. This explains why the disturbance propagates downwards through to the passage below, while the growth in the passages above remains constrained. This can be seen by drawing a line between comparable features in the downstream wakes, and is illustrated for $t = 5.0$.

⁴The acoustic waves propagate at speeds of $u \pm Ma \in [0.7, 1.3]$, while the convective speed is $Mc \approx 0.3$.

At intermediate timescales, between approximately $t = 5.0$ and $t = 10.0$, the main receptivity mechanism begins to operate and propagate the disturbance throughout the domain. This can be observed in Fig. 4 by the successive growth in the lengths of the wakes from the perturbed blade and downwards (shown with a line for the $t = 5.0$ panel), although at this point the asymptotic ($t \rightarrow \infty$) phase relationship in the pressure dynamics between the blades is not yet fully established. Localized wave packets of intensified acoustic radiation are observed periodically emanating from the blades, followed by periods of quiescence (see the region $x < 0, y \in [0, 3]$ at $t = 5.0$ and $t = 7.0$ of Fig. 4), which is consistent once again with the beating mechanism observed previously and occurring, according to Fig. 5, at similar timescales to those observed in the single-passage impulse response. It thus suggests that this growth occurs through local feedback mechanisms on the surfaces of the blades observed in the single-passage setting.

Here we also observe the establishment of large-scale structures. Throughout Fig. 4 a slowly moving region of approximately five to six passages propagates downwards, characterized by wavefronts angled at approximately 45° from the axis of the blade row. Although a definitive description awaits further analysis, the fact that it appears above the perturbed blade suggests that the mechanism at play is related to scattered acoustic waves, as these are the only structures capable of bypassing the asymptotically dominant receptivity mechanism, which, as we have mentioned extensively, is mostly a localized interaction.

We can explain the persistence of this structure by noting that it, like the dominant mechanism, propagates downwards one passage at a time, potentially through similar receptivity mechanisms as discussed above, given the similarity of the acoustic wavelengths between single-passage M_0 and this structure. As such, the timescales for the feedback are similar, and so the “group velocity” of both structures through the cascade are comparable.

The dephased wave packet is eventually dominated by the structure with a constant acoustic-source phase relationship, as is seen developing on the blade surfaces at $t = 20.0$. This seems reasonable because each blade has identical receptivity characteristics, by construction. Structures with constant phase relationships between the passages are therefore expected to dominate, with frequencies and growth rates dictated by the geometry of the problem. For asymptotically large times ($t \rightarrow \infty$), the most unstable eigenvalue dominates. Based on our earlier investigations we expect this system to be unstable, with *at least* the same growth rate as the single passage, following our observations of the spectral structure of the N -periodic system in Sec. II B. In fact, an exponential fit of the norm growth rate between $t = 10 \rightarrow 20$ shows a growth rate of $\text{Re}\{\lambda\} = 0.390$, which is higher than that observed in the single passage. The corresponding snapshot at $t = 20$, in Fig. 4, confirms that this is a full 10-periodic structure and that the mode is, at least qualitatively, similar to that seen in the single passage with a near-constant phase shift between each consecutive passage. This justifies the analysis of the N -periodic configuration, since it clearly demonstrates that our system contains dynamics that are substantially different from, and impossible to model in, the single-passage. Modeling larger sectors of the bladed disk are naturally expected to produce additional, larger-period modes and behaviors, but this paper concentrates on a 10-periodic sector in order to reduce the associated (and sizable) computational costs.

D. Global stability

Global spectra are obtained directly from the definition above, using the triplet system in Eq. (10), by applying the SLEPC methodology introduced in part I. We observe that, for an eigenvalue-eigenvector pair $(\lambda_j, \mathbf{v}_j)$ of the triplet system for a root of unity ρ_j , the vector $\mathbf{v} = (\mathbf{v}_j, \rho_j \mathbf{v}_j, \dots, \rho_j^{N-1} \mathbf{v}_j)^\top$ is an eigenvector of the full N -periodic system matrix \mathbf{A} , with similar results for the adjoint operator following directly.

Note that, since $\mathbf{P}^H \mathbf{A} \mathbf{P} = \hat{\mathbf{A}}$, taking the Hermitian conjugate of both sides results in $\mathbf{P}^H \mathbf{A}^H \mathbf{P} = \hat{\mathbf{A}}^H$. This shows that the same process can be used to compute the adjoint modes alongside the direct eigenvectors, and that, since $\mathbf{w} = (\mathbf{w}_j, \rho_j \mathbf{w}_j, \dots, \rho_j^{N-1} \mathbf{w}_j)^\top$, in the inner product $\langle \mathbf{w}, \mathbf{v} \rangle_{\mathbf{M}}$ the conjugation of \mathbf{w} would result in the multiplication $\bar{\rho}_j \rho_j = 1$ in each passage. It hence follows that

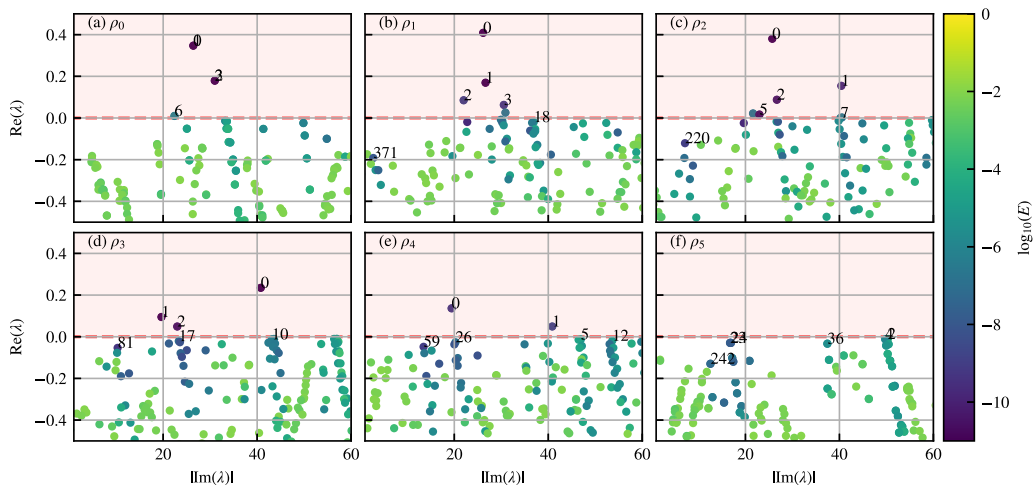


FIG. 6. The 10-periodic direct modes for the five nonsymmetric roots of unity. Note the absence of any new unstable structures for ρ_5 , which means that the two-periodic system has the same unstable modes as the single-passage case.

the *wavemaker is invariant with respect to the passage*, and so the wavemakers in what follows will be presented within a single-passage domain only.

1. Direct spectra

The direct spectrum is calculated for the roots of unity $\{\rho_j\}_{j=1}^9$, and focusing primarily on the modes with frequencies $|\text{Im}\{\lambda\}| < 60$, $\text{Im}\{\lambda\} \neq 0$. This is because we have identified the most unstable eigenvalue to be in this region in [1], and because we expect large-scale structures (with wavelengths on the order of $10h_p$), such as the one observed in the upstream region of the impulse response, to manifest with low temporal frequencies (e.g. $|\text{Im}\{\lambda\}| \lesssim 20.0$).

Instead of considering the modes for each ρ_j sequentially, we are rather interested in how a given mode in the one-periodic case (i.e., the fields corresponding to modes in ρ_0) changes based on the periodicity of the problem as we move ρ_j along the boundary of the unit circle. In other words, we interpret the N -periodic analysis as a map of the unit circle onto the closed curve $\text{eig}(\hat{A}(e^{i\theta}))$, onto which the discrete roots of unity $\rho_j = e^{2\pi i \theta_j / N}$ are mapped as well.

We can illustrate this mapping on a smaller toy problem by plotting out the symbol curve of $\hat{\mathbf{T}}(z) = \mathbf{T}_0 + z\mathbf{T}_1 + \mathbf{T}_{N-1}/z$, for points on the unit circle $z = e^{i\theta}$, representing all the possible roots of unity, for all possible $N \in \mathbb{N}$. With an arbitrary choice of 3×3 matrices,⁵ $\hat{\mathbf{T}}(z)$ is shown for the three eigenvalues in each case in Fig. 7. Each of the eigenvalues follows its own path through the complex λ space. This example clearly shows that while the “single-element” problem is stable, the addition of other “elements” can lead to the system becoming unstable with the dominant structure in the dynamics alternating between different mode families (e.g., compare the most unstable eigenvalue in $N = 2$ against $N = 3$ in Fig. 7).

For the aerofoil case, the problem appears to be effectively symmetric about ρ_5 , which may be due to the flow being essentially uniform and parallel to the mesh boundaries at which the periodic

⁵The toy-problem matrices are $\mathbf{T}_0 = -\begin{pmatrix} 3/2 - 2i & 0 & 0 \\ 0 & 1/2 + 4i & 0 \\ 0 & 0 & 3 \end{pmatrix}$, $\mathbf{T}_1 = -\begin{pmatrix} -1 & 1 & -1 \\ 0 & -1 & 1 \\ -1 & 0 & 1 \end{pmatrix}$ and $\mathbf{T}_{N-1} = -\begin{pmatrix} 0 & -1 & -1 \\ 1 - i & 0 & 1 \\ -1 & 1 - i & 0 \end{pmatrix}$.

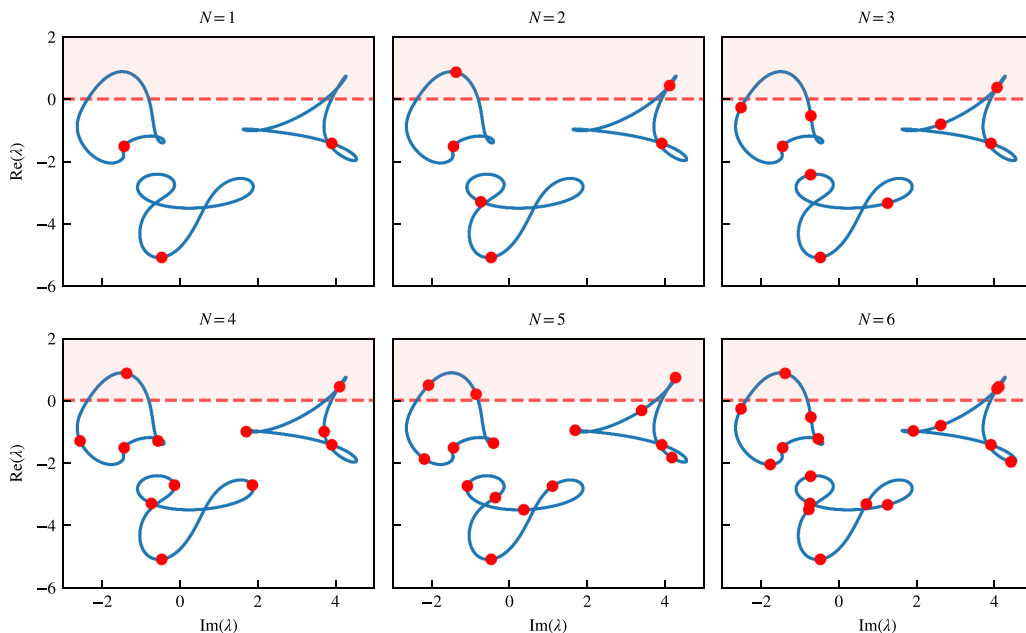


FIG. 7. Mapping of the unit circle $z = e^{i\theta}$ onto the curve $\text{eig}(\hat{A}(z))$. With our choice of $\mathbf{T}_0, \mathbf{T}_1, \mathbf{T}_{N-1}$ the eigenvalues traverse separate curves, shown in blue. Each panel presents the mapping of the roots of unity for a given N , shown in red.

boundary condition is applied, although the exact cause of this feature warrants future investigation. As a result, we will look only at modes for $\rho_0 \rightarrow \rho_5$ in the analysis presented here. We observe that there are no additional unstable two-periodic modes (ρ_5) in Fig. 6. Since the spectrum for the two periodic problem is the union of the ρ_0 and ρ_5 spectra, it follows that the dominant structures observed for this case would give the same response as a single passage. This may lead to false conclusions regarding the dynamics of multibladed systems when simulations that are performed on a two-passage mesh do not show de-synchronization of the passages.

2. Most unstable modes

Let us first consider the most unstable mode (ρ_0, M_0) . From Fig. 6, this mode becomes more unstable in the five- (ρ_2) and 10-periodic (ρ_1) cases compared to the one-periodic passage, with the growth rate increasing from $\text{Re}\{\lambda\} = 0.347$, for (ρ_0, M_0) , to $\text{Re}\{\lambda\} = 0.380$, for (ρ_2, M_0) , and finally to $\text{Re}\{\lambda\} = 0.408$, for (ρ_1, M_0) .⁶ The visualization of these modes in Fig. 8 shows that, as the periodicity is increased, the wavefronts of the upstream acoustic field deviate away from the vertical plane waves seen for ρ_0 , as expected, due to the changing phase relationship defined through the N -periodic decomposition. We also observe that the form of the most unstable mode, (ρ_1, M_0) in Fig. 8, matches the asymptotic behavior of Fig. 4. The only difference is that the asymptotic growth rate of 0.390, determined in Fig. 5, is lower than the eigenvalue growth rate $\text{Re}\{\lambda\} = 0.408$. This is attributable to the length of the impulse response simulation and the slow decay of the low-frequency dynamics associated with the dephased wave packet, which even at $T = 20$ is still not saturated by the most unstable mode. Based on these growth rates, it is reasonable to assume that the real part of the mapping of the unit circle onto the symbol curve grows for small arguments θ before gradually

⁶The modes are $(\rho_0, M_0) = 0.409 - 26.143i$, $(\rho_1, M_0) = 0.409 - 26.143i$ and $(\rho_2, M_0) = 0.380 - 25.714i$.

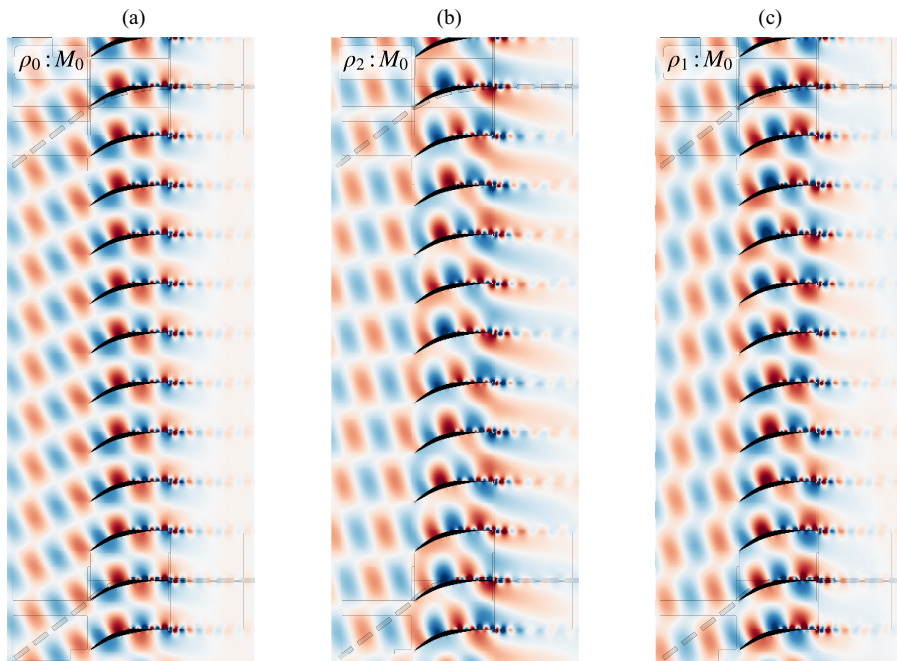


FIG. 8. The most unstable pressure modes in the (a) single, (b) five-periodic, and (c) 10-periodic cases, showing an adjustment of the upstream wavefronts to a more oblique configuration alongside dominant suction-side dynamics on the surface of the aerofoil.

decreasing as the argument increases. However, with only the one-, two-, five-, and 10-periodic solutions resolved with this analysis, it is not possible to obtain the exact mapping of the unit circle onto the symbol curve, in a manner similar to that shown in the demonstration example of Fig. 7. By choosing a highly composite number,⁷ further resolution can be achieved, thereby allowing for a more detailed interpretation of the effects of having more blades within the blade row; the downside of this approach is increased cost, albeit one that increases linearly with N .

Continuing with the analysis, the pressure distributions for the three scaled modes are shown in Fig. 9. Peak pressure amplitudes are consistently higher for the 10-periodic case when compared to the five-periodic configuration on the suction surface, with higher pressures seen for the five-periodic case only on the pressure surface for $x > 0.9$. On the suction side, pressures for (ρ_0, M_0) are higher than the high-periodicity modes for $x < 0.220$, with the latter dominant for $0.220 \leq x \leq 0.507$. Crucially, (ρ_1, M_0) attains higher amplitudes ($\sim 5\%$ higher) at the point of peak sensitivity, at $x = 0.273$, as evidenced by the adjoint fields. Downstream of $x = 0.507$, the peak pressures of (ρ_0, M_0) increase and are greater than those of (ρ_2, M_0) , and comparable to those of (ρ_1, M_0) ($|p| \approx 3.356 \times 10^{-2}$). Note also that peaks in $x > 0.507$, corresponding to ρ_1 and ρ_2 , show small displacements in x due to the changes in the standing wave pattern resulting from the small variations in frequency between the modes.

Adjoint fields demonstrate reduced sensitivity for the N -periodic modes on both the suction and pressure surfaces, but the deficit is reduced when the wavemaker is calculated, as shown in Fig. 9(b). The wavemakers show that the (ρ_0, M_0) mode has the greatest structural sensitivity, with sensitivity

⁷A highly composite number is one that has a large number of divisors. This means that many periodicities are captured by a periodic analysis. For example, $N = 10$ has divisors 1, 2, 5, 10, while $N = 12$ has 1, 2, 3, 4, 6, 12.

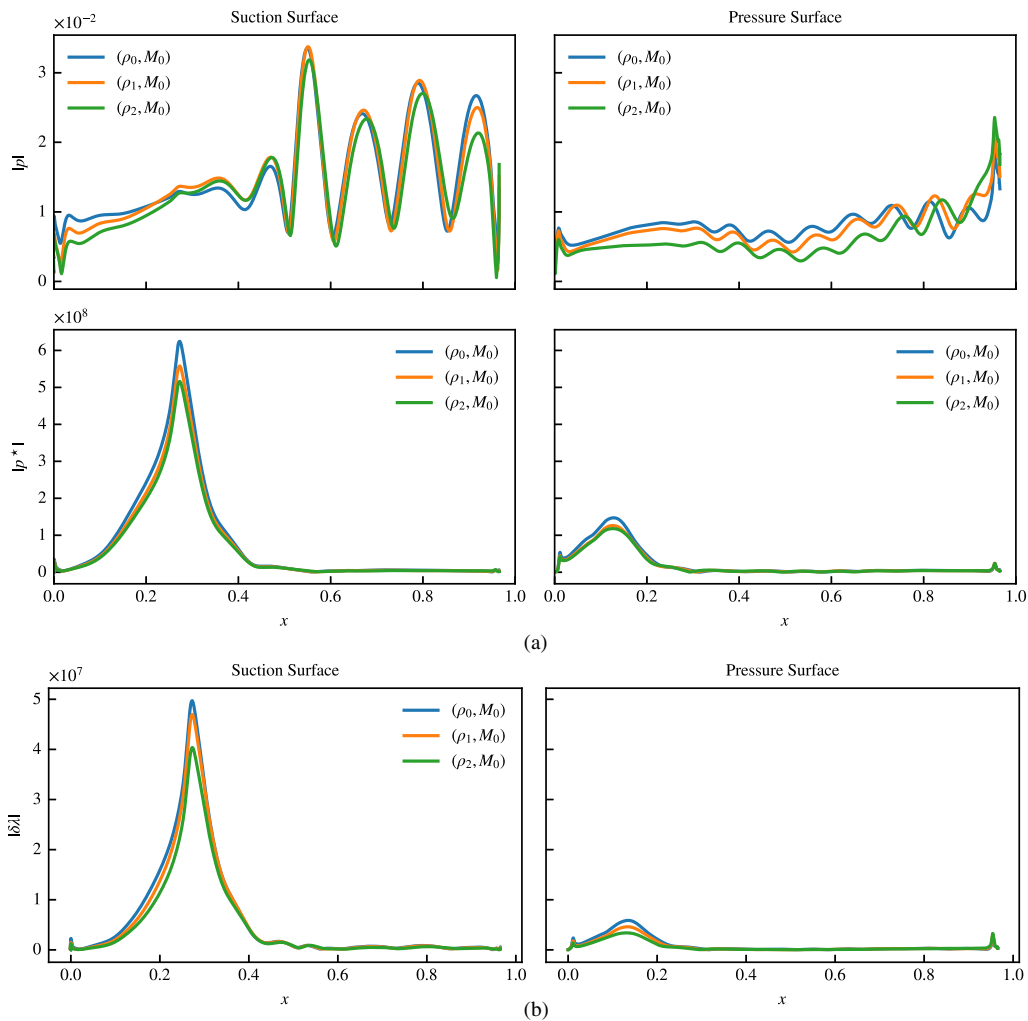


FIG. 9. The surface direct and adjoint pressure distributions for the modes (ρ_0, M_0) , (ρ_1, M_0) , and (ρ_2, M_0) in (a), and the corresponding wavenumbers in (b).

decreasing while traversing the unit circle (i.e., as $\arg(\rho)$ increases). It is important to note, however, that a lower value of the wavenumber field is not necessarily indicative of a less dominant structure, only one that is less sensitive. Highly amplified robust structures may therefore result in lower wavenumber fields, which could be the process that leads to smaller wavenumber peaks for (ρ_1, M_0) and (ρ_2, M_0) .

The effect of changing the argument of ρ is to alter the phase relationship between the pressure and suction surfaces. By changing ρ , the phase relationship may become more optimal between the features on the suction and pressure surfaces; this possibility requires further study and greater resolution in θ to verify. Furthermore, we have seen in the impulse response analysis, carried out above, that the system is defined by convective and acoustic timescales. Hence determining the dominant modes may involve considering the phase relationships at the point of receptivity *and* the form of the resulting waves as they interact at the trailing edge. For this reason, an acoustic ray-tracing argument should be adopted to further explore the relationship between periodicity and modal growth rates.

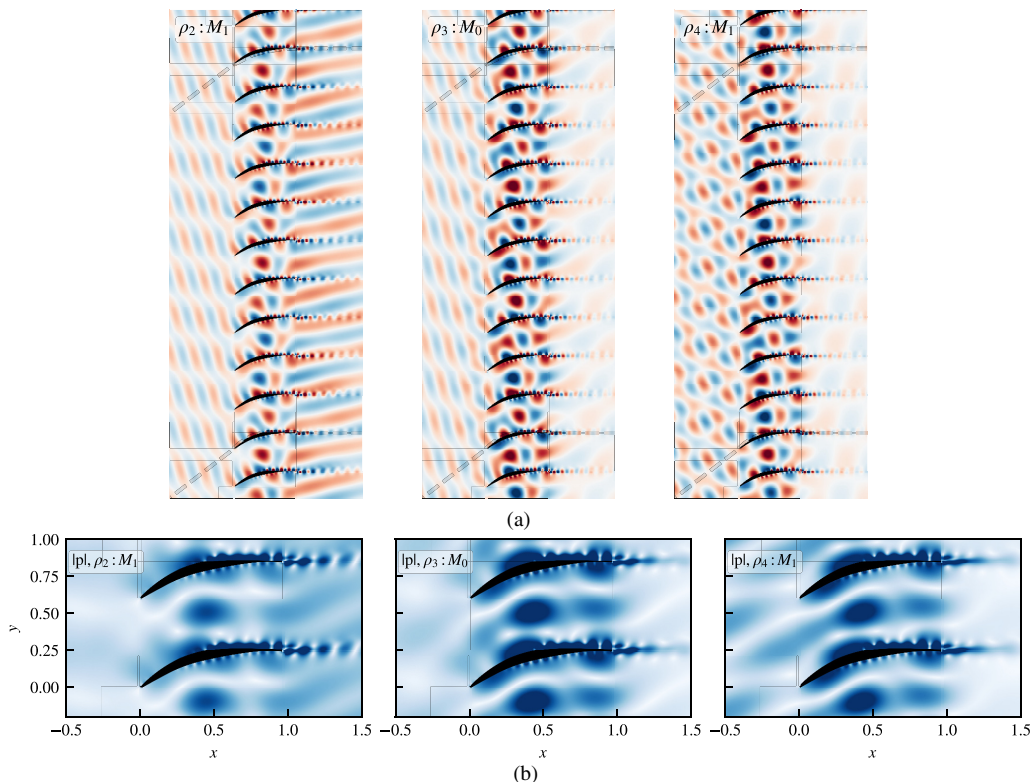


FIG. 10. Pressure fields for (ρ_2, M_1) , (ρ_3, M_0) , and (ρ_4, M_1) in (a), with the pressure amplitudes within the passage shown in (b). In (b) note the high-pressure amplitudes within the passage in (ρ_3, M_0) , and the appearance of pressure structures in the downstream and upstream of (ρ_2, M_1) and (ρ_4, M_1) , respectively.

3. Unstable structures

The higher periodicity also leads to unstable resonance structures that trap acoustic waves within the blade passages, reminiscent of Parker modes. This mode family is seen for $(\rho_2, M_1) = 0.154 - 40.402i$, $(\rho_3, M_0) = 0.235 - 40.769i$ and $(\rho_4, M_1) = 0.0493 - 40.838i$. While a trapped acoustic mode is seen within the blade passages for all these modes, note how the change in periodicity in (ρ_3, M_0) concentrates the mode within the passage by removing propagating waves in the upstream and downstream regions, and that this corresponds to the most unstable mode of this group. We recall from Fig. 6 that there are no unstable modes for ρ_0 in this frequency range, and hence this example demonstrates the appearance of families of modes that are captured in our multipassage setting. The modes discussed here, and the pressure amplitudes highlighting the trapped acoustic waves, are shown in Fig. 10.

4. Low-frequency dynamics

Low-frequency dynamics are also captured in our analysis, with a spectrum that is significantly denser in $|\text{Im}\{\lambda\}| < 20$ for all ρ_i where $i \neq 0$, in comparison to ρ_0 . Despite the challenges of converging these modes, we have been able to select the sufficiently well converged modes (ρ_1, M_{371}) , (ρ_2, M_{220}) , (ρ_3, M_{81}) , (ρ_4, M_{59}) , and (ρ_5, M_{242}) , so as to visualize the low-frequency dynamics here. These modes are shown in Fig. 11, and, in all cases shown here, the pressure dynamics of the modes exhibit large-scale plane-wave structures that span multiple passages, both upstream and downstream of the blade row. Furthermore, unlike the modes seen previously in this paper, the

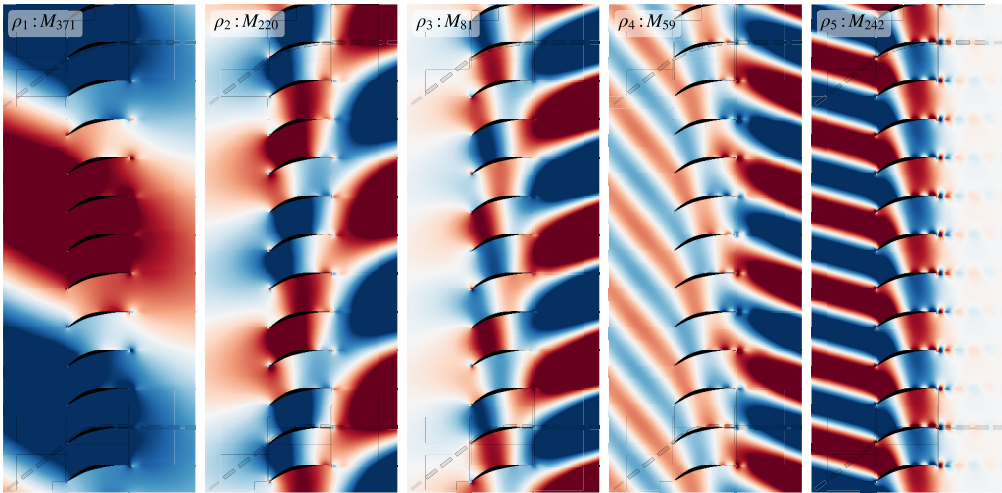


FIG. 11. Selected low-frequency acoustic modes of the 10-periodic linear cascade.

acoustic mode structure within the passages takes the form of plane waves with wavelengths greater than 1.

To determine the driver of these acoustic dynamics, plots of the speed, $|\mathbf{u}|$, in Fig. 12, show the hydrodynamics localized at the blade surface. In essence, the unsteady hydrodynamic activity is confined to the suction-side boundary layer and within the wake downstream of the trailing edge. For the lowest-frequency mode considered here, (ρ_1, M_{371}) , these dynamics take the form of acoustic plane waves occupying the upstream portion of the domain and driven by a low-frequency ($\text{Im}\{\lambda\} = 2.76$) “flapping” motion of the suction-side laminar separation bubble. In contrast, the other modes,

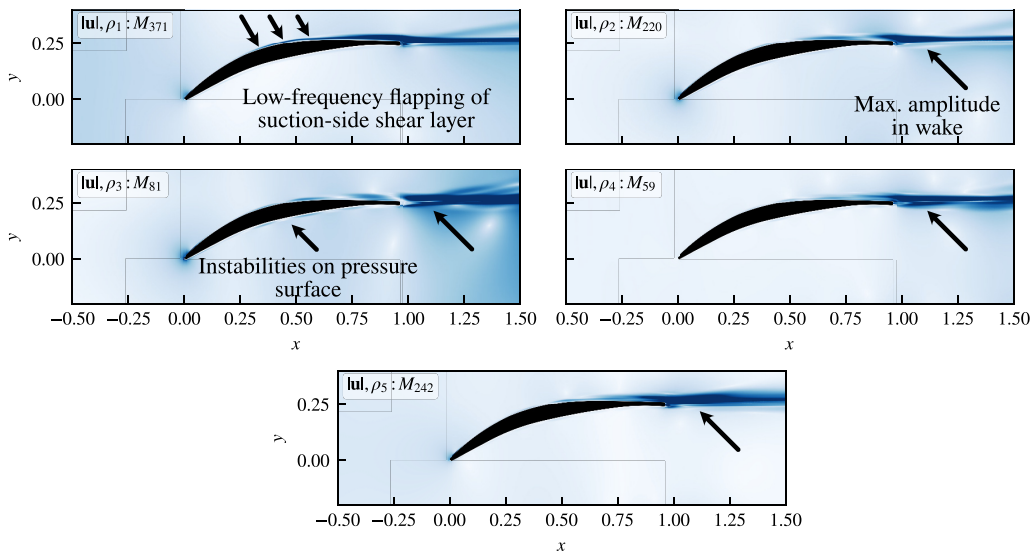


FIG. 12. Plots of the speed fields $|\mathbf{u}|$ for the low-frequency modes. Arrows indicate high-amplitude disturbances in the near wake, while for (ρ_1, M_{371}) , the arrows show low-frequency flapping on the suction surface.

with higher frequencies, localize their fluctuations closer to the trailing-edge and the near-wake regions.

The selected modes in Fig. 6, especially (ρ_1, M_{371}) , are located in regions of the spectrum that are surrounded by other modes with poorer convergence characteristics, although ones that are suggestive of higher growth rates. As such, while we have been able to observe low-frequency structures in these modes, further analysis, including a careful receptivity study, are required for a more complete understanding of the hydrodynamic features driving these modes. This can be achieved by using a combination of shift-invert and harmonic extraction techniques to target the low-frequency branches of the spectrum.

III. CONCLUSION

This second part of our two-part paper extended the modal and nonmodal aeroacoustic stability analysis of a representative single-blade passage at $\text{Re} = 100\,000$ and $M = 0.3$ to a 10-periodic configuration. Using a cyclic decomposition of the system matrix, we demonstrated how a tuned N -periodic blade row problem may be decomposed into smaller subproblems that enable computationally tractable stability calculations for cascades of arbitrary sizes by making use of the properties of block-circulant matrices.

Through the use of this method, the single-passage analysis was replicated for a 10-periodic linear blade row. The impulse-response analysis showed that disturbances propagate through this linear cascade by exploiting suction-side sensitivities that are exposed to the dipole source at the trailing edge of the blade above. Scattering of an initial pressure pulse by the leading edges of the cascade blades also resulted in the formation of a persistent transient region occupying five passages. This region is characterized by weak acoustic radiation in the upstream and a perturbed wave vector. The persistence of this feature was explained by the same suction-side propagation arguments. These observations are summarized in Fig. 13(c).

This analysis of the N -periodic system represents a first attempt at a detailed global stability analysis of a linear cascade configuration with $N > 1$ with emphasis on acoustically driven feedback mechanisms. By extending the calculation to 10 passages, it was shown that the local feedback mechanisms that exist in the single-passage case can result in the formation of large-scale synchronization structures that span the entire blade row. These structures are shown to arise due to the interaction of acoustic sources with neighboring blades—a feature that cannot be resolved by single-passage impulse-response analyses, such as those presented in [19]. Due to the absence of shocks in this model compressor blade row, blade-to-blade interactions in our study are more complex than in the high-pressure turbine simulations in [19], as acoustic perturbations can travel further upstream and hence interact with blades both above and below, as shown in Fig. 13.

The direct and adjoint spectra for the 10-periodic problem were also obtained successfully. From this, we concluded that the 10-periodic domain accommodates a more unstable dynamics that supersede the most unstable mode for the single passage. Low-frequency modes were also obtained and analyzed using adjoint quantities and the wavemaker concept. Of more practical interest, however, is the observation that the two-periodic system does not admit any additional unstable modes, which demonstrates that computational solutions seeking to investigate flow instabilities in one or two passages may fail to capture the dynamics of the full N -periodic system, even if the one- and two-passage solutions have the same dominant dynamics. Instead, an analysis of the type presented here is required to represent the full flow behavior including local instabilities, receptivity points, feedback loops, beating and synchronization effects, and their complex interactions.

In this work we have restricted ourselves to considering multipassage configurations where the geometry and mean flow field in each passage are identical: a so-called “tuned” state. In reality, working machinery rarely satisfies this assumption. Instead, these blades may be *mistuned* in some way, such as in their mechanical properties, stagger angle, pitch height, surface geometry, or the effects of other components of the machine altering the mean flow in some portion of the cascade. This can be by design, as a result of wear and damage to the aerodynamic surfaces, or due to blade

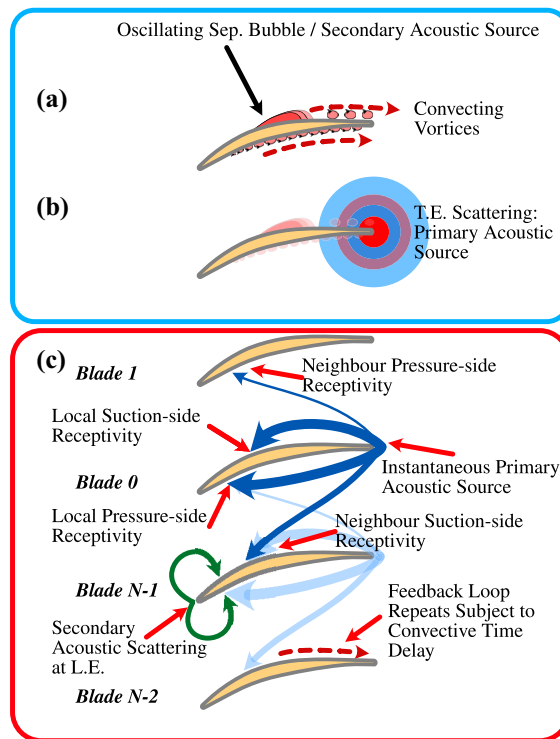


FIG. 13. The local and global feedback mechanisms identified for N -periodic geometries in this paper.

untwist altering the stagger angles of individual blades under the applied aerodynamic loads. Prior work on mistuned periodic assemblies has suggested that small amounts of mistuning can result in mode localization and eigenvalue veering phenomena in systems where the oscillating substructures are weakly coupled. A brief overview and discussion of this is presented in Appendix C of [20], although further work is required to adapt the present method to these situations.

ACKNOWLEDGMENTS

The authors gratefully acknowledge financial support from Ministerio de Economía y Competitividad AEI/FEDER UE through Grant No. DPI2016-75777-R, and the UK Turbulence Consortium. This work used the ARCHER and ARCHER2 UK National Supercomputing Service.

APPENDIX: DETAILS OF COMPUTER WALL TIMES

All numerical calculations within this paper require the use of high-performance computing (HPC) facilities, and therefore it bears a brief mention of how this is achieved here.

Calculations in part I of our paper use the FinisTerra II supercomputer provided by CESGA, using 2.5GHz Intel Xeon E5-2680v3 (Haswell) processors, while the results in this part are obtained primarily using the Edinburgh Parallel Computing Centre (EPCC) ARCHER system, which used 2.7 GHz Intel Xeon E5-2697 (Ivy Bridge) processors, although some additional results were also obtained using the implementation phase of the successor system, ARCHER2.

The single-passage mesh described above is the basis for all calculations in this paper. For the fast nonlinear cases, the simulations are run on 80 processors, with 20 in the horizontal/axial and four in the vertical/pitchwise directions, and amounts to a load of 22 528 degrees of freedom per

TABLE I. Computer resource utilization for the different cases shown in both parts of this two-part paper.

	Case	Grid Size	Procs.	Wall Time (h)	CPUh
Single passage	Nonlinear		80	07:56	635
	Impulse response	450 560		09:18	744
	Direct eigenvalues		164	17:00	2788
	Adjoint eigenvalues			48:00	4873
Impulse response			~08:30 (avg)	~48 734 (total)	
Multiple passages	Direct eigenvalues	1 351 680	492	~20:48 (avg)	~102 336 (total)
	Adjoint eigenvalues			~27:40 (avg)	~136 120 (total)

processor. For the larger eigenvalue calculations, this is increased to 164 processors in a 41×4 distribution, which was found to give sufficiently fast turn-around times.

For the multipassage problem in Sec. II, the methodology consists of performing similar calculations on three identical passages that are stacked pitchwise. Processor loading and distributions are identical in this case, with 492 ($= 3 \times 164$) processors used. It appears that the single-passage adjoint eigenvalue calculation was bottle-necked by disk write speeds for the simulation that returned >2000 eigenvalues, and hence terminated after 48 hours. A later test simulation produced a nominal runtime of 34:00, where the number of returned vectors was limited to 65. This seems to have been a problem with the HDF5 library on FinisTerra II, since a reinstallation of the code on ARCHER results in “multiple-passage” figures that suggest a scaling between the direct and adjoint closer to 1.3. This is larger than the maximum direct-adjoint scaling factor of 1.1 observed in [21], and suggests that there may be additional performance losses incurred in either IO performance or through the amended N -periodic structuring of the right-hand side function (see Sec. II B for additional details), the latter of which is more likely here.

A summary of computational times and costs is given in Table I.

At realistic operating conditions, which typically occur with higher Reynolds on the order of $Re \approx 10^6$, the associated mesh resolution requirements scale as $N \approx Re^{37/14}$ for DNS, and as $N \approx Re^{13/7}$ in wall-resolved LES [22], from which it follows that a transition of the present analysis to three-dimensional calculations would incur significant penalties in terms of the number of floating-point operations from both the refined grid and the reduced time step.

Nominally the computational cost of the N -periodic methodology depends only on N , but this somewhat masks the data rearrangement step of the triad, as described in Sec. II B. With a greater number of degrees of freedom in each passage, the communication step will become more expensive, and hence the scaling relationships in Table I will degrade; however, this may be mitigated with better data management techniques that have not been explored in this paper.

-
- [1] A. Glazkov, M. F. de Pando, P. J. Schmid, and L. He, preceding paper, Global stability analysis of an idealized compressor blade row. I. Single-blade passage analysis, *Phys. Rev. Fluids* **8**, 103903 (2023).
[2] L. He and W. Ning, Efficient approach for analysis of unsteady viscous flows in turbomachines, *AIAA J.* **36**, 2005 (1998).

-
- [3] K. C. Hall, J. P. Thomas, and W. S. Clark, Computation of unsteady nonlinear flows in cascades using a harmonic balance technique, *AIAA J.* **40**, 879 (2002).
- [4] K. Ekici and K. C. Hall, Nonlinear analysis of unsteady flows in multistage turbomachines using harmonic balance, *AIAA J.* **45**, 1047 (2007).
- [5] A. Gopinath, E. van der Weide, J. Alonso, A. Jameson, K. Ekici, and K. Hall, Three-dimensional unsteady multi-stage turbomachinery simulations using the harmonic balance technique, *45th AIAA Aerospace Sciences Meeting and Exhibit* (American Institute of Aeronautics and Astronautics, 2007).
- [6] J. I. Erdos, E. Alzner, and W. McNally, Numerical solution of periodic transonic flow through a fan stage, *AIAA J.* **15**, 1559 (1977).
- [7] L. He, An Euler solution for unsteady flows around oscillating blades, *J. Turbomach.* **112**, 714 (1990).
- [8] L. He, Method of simulating unsteady turbomachinery flows with multiple perturbations, *AIAA J.* **30**, 2730 (1992).
- [9] G. A. Gerolymos, G. J. Michon, and J. Neubauer, Analysis and application of chorochronic periodicity in turbomachinery rotor/stator interaction computations, *J. Propul. Power* **18**, 1139 (2002).
- [10] P. J. Schmid, M. F. de Pando, and N. Peake, Stability analysis for n -periodic arrays of fluid systems, *Phys. Rev. Fluids* **2**, 113902 (2017).
- [11] F. Bloch, Über die Quantenmechanik der Elektronen in Kristallgittern, *Z. Phys.* **52**, 555 (1929).
- [12] B. Olson, S. Shaw, C. Shi, C. Pierre, R. Parker, R. P. Circulant, B. J. Olson, S. W. Shaw, L. S. Randolph, and D. Head, Circulant matrices and their application to vibration analysis, *Appl. Mech. Rev.* **66**, 040803 (2014).
- [13] B. Hellmich and J. R. Seume, Causes of acoustic resonance in a high-speed axial compressor, *J. Turbomach.* **130**, 031003 (2008).
- [14] R. Parker, Resonance effects in wake shedding from compressor blading, *J. Sound Vib.* **6**, 302 (1967).
- [15] R. Parker, Acoustic resonances and blade vibration in axial flow compressors, *J. Sound Vib.* **92**, 529 (1984).
- [16] R. Parker and S. Stoneman, An experimental investigation of the generation and consequences of acoustic waves in an axial flow compressor: Large axial spacings between blade rows, *J. Sound Vib.* **99**, 169 (1985).
- [17] R. Parker and S. A. T. Stoneman, The excitation and consequences of acoustic resonances in enclosed fluid flow around solid bodies, *Proc. Inst. Mech. Eng. C: Mech. Eng. Sci.* **203**, 9 (1989).
- [18] See Supplemental Material at <http://link.aps.org/supplemental/10.1103/PhysRevFluids.8.103904> for Movie of linear impulse response in a tuned 10-passage blade row.
- [19] R. Sandberg and A. Wheeler, Effect of trailing-edge boundary conditions on acoustic feedback loops in high-pressure turbines, *J. Sound Vib.* **461**, 114917 (2019).
- [20] A. Glazkov, A direct-adjoint framework for stability and sensitivity analyses of turbomachinery aeroacoustics, Ph.D. thesis, University of Oxford, 2021.
- [21] M. Fosas de Pando, D. Sipp, and P. J. Schmid, Efficient evaluation of the direct and adjoint linearized dynamics from compressible flow solvers, *J. Comput. Phys.* **231**, 7739 (2012).
- [22] H. Choi and P. Moin, Grid-point requirements for Large Eddy simulation: Chapman's estimates revisited, *Phys. Fluids* **24**, 011702 (2012).